RSC Advances

PAPER

View Article Online
View Journal | View Issue

Cite this: *RSC Adv.*, 2026, **16**, 19752

Multi-enzyme mimic Mn_3O_4@SiO_2 nanoparticles for efficient anti-inflammation therapy

Liang Chen,[a] Lulu Fang,[a] Haitao Lin,[a] Yanzhe Ge,[a] Yuan Cheng[b] and Jianquan Wang *[c]

Received 28th December 2025
Accepted 3rd April 2026

DOI: 10.1039/d5ra10050j

rsc.li/rsc-advances

The global prevalence of gingivitis has raised the cost considerably for extensive healthcare and refractory management, which is often accompanied by excessive accumulation of reactive oxygen species (ROS) that are considered to play a pivotal role in the development of gingivitis and other inflammatory diseases. Ordinary medications for the treatment of gingivitis, such as chemical anti-inflammatory or antimicrobial agents, are sometimes unsatisfactory due to rapid pathogen consumption and metabolism. To this end, new strategies and platforms are thus needed for the treatment of such ROS-related diseases. Herein, Mn_3O_4@SiO_2 NPs were designed and prepared through an *in situ* templating method and were found to possess over 2.5 times the *in vivo* antioxidant removal capacity and a 3-fold TNF (tumor necrosis factor)-α sequestration efficacy when compared with Mn_3O_4 NPs at the same concentration of Mn_3O_4. This was achieved through efficient catalytic ROS scavenging, thanks to the enlargement of the surface area and the enhanced dispersity and stabilization of the mesoporous SiO_2-supported Mn_3O_4 NPs. Furthermore, 65% of the IL (interleukin)-1β was down-regulated by the Mn_3O_4@SiO_2 NPs compared with an untreated gingivitis mouse model group, and in contrast, the IL-1β suppression rate for the iso-stoichiometric Mn_3O_4 NPs was about 85%. The multi-enzyme mimicking Mn_3O_4@SiO_2 NPs provided satisfactory biosafety and therapeutic effects in a gingivitis mouse model and thus represent a promising therapeutic platform for treating gingivitis and other inflammatory diseases.

1. Introduction

Gingivitis is one of the most prevalent periodontal disorders, manifested as gum oedema, erythema, swelling, pain and bleeding, which often arises from bacterial infection, trauma, and allergic reactions.[1,2] Gingivitis is usually self-limited; however, if not well-managed, it may progress to periodontitis, a more severe condition that causes tooth loosening, instability, eventual tooth loss, and maxillofacial destruction.[3,4] Conventional treatment of gingivitis in clinical trials includes antimicrobial and chemical agents for bacterial suppression, reduction of inflammation and immunomodulation.[5–7] However, the outcomes of such treatments are substantially restricted due to drug resistance and low bioavailability.[8] Based on the inadequacy of traditional remedies, there is an urgent need for the development of new therapeutic agents and platforms to effectively treat and manage gingivitis.

As a typical inflammatory process, gingivitis shares the fundamental characteristics of inflammation pathology, such as elevated production of reactive oxygen species (ROS), including hydrogen peroxide (H_2O_2), hydroxyl radicals ($^{\bullet}OH$), and superoxide anion radicals ($^{\bullet}O_2^-$), which are mostly generated by both innate and adaptive immune cells during the process of host defense.[9,10] ROS are crucial for confronting infection; however, an excessive amount has been shown to be harmful to normal tissue and bring about secondary side effects.[11–13] To this end, a naturally occurring negative feedback mechanism has developed, represented by endogenous antioxidant enzymes, such as superoxide dismutase (SOD), catalase (CAT), and glutathione peroxidase (GPx), which play a vital role in cyto-protection as ROS scavengers, thus maintaining the overall cellular redox balance.[14] The ROS-eliminating efficiency of autologous antioxidant enzymes is generally insufficient when encountering pathological inflammation like gingivitis, while heterologous pharmaceutical enzymes may involve an immune response and rejection.[15] To fill this gap, alternative antioxidant enzymes or other therapeutic agents with low immunogenicity have been designed and exploited for preclinical study and treatment of inflammatory diseases.

In the last decade, a range of nanostructured materials with intrinsic antioxidant enzyme-mimicking activity have been reported, thanks to the rapid advances of nanotechnology.[16–23] These enzyme mimics are preferred over natural counterparts because they offer numerous advantages, such as higher

[a]*Department of Oral and Maxillofacial Surgery, Yi Ji Shan Hospital of Wannan Medical College, Wuhu, Anhui, China*

[b]*Wuxi Xishan NJU Institute of Applied Biotechnology, Wuxi 214104, China*

[c]*College of Materials Engineering, Jinling Institute of Technology, Nanjing 211169, P. R. China. E-mail: wangjianquan006@163.com*

stability, better design flexibility, and surface chemistry tunability. These mimics are known as "nanozymes"[15,24,25] and have been extensively explored for a range of biomedical applications, ranging from cell protection, wound repair, anti-aging treatment, anti-inflammation treatment, and anti-cancer treatment.[25–28] Among them, Mn-based nano-materials are promising due to their multi-valency, favorable biodegradability and biocompatibility. Even though the *in vivo* anti-inflammation capacity of Mn_3O_4 has been reported, its hydro-dispersibility, which profoundly influences its catalytic activity, needs further improvement.[18,19] The active site on the surface of an enzyme-mimic nano-material would be blocked when it is aggregated, which hinders the "touch and go" process by which the substrate participates in enzymatic reactions.[29]

To fulfill the above demands, in this work, Mn_3O_4 nano-particles (NPs) were *in situ* synthesized and scattered in mesoporous SiO_2 nano-templates, and the as-prepared Mn_3O_4 NPs were embedded and fixed in the porous apertures of SiO_2 NPs with "isolated island" status, as shown in Scheme 1. The resulting Mn_3O_4@SiO_2 NPs could eventually enhance the overall specific surface area and stability of the Mn_3O_4 NPs that are essential for multiple ROS elimination. The *in vitro* and *in vivo* studies showed that the Mn_3O_4@SiO_2 NPs designed and prepared in this work possessed multi-enzyme mimic activities that surpassed Mn_3O_4 NPs under the same stoichiometric dosage, and significantly reduced the ROS, so that a gingivitis mouse model was ameliorated with satisfactory biocompatibility. The results indicated that the Mn_3O_4@SiO_2 NPs in this work could provide a promising strategy for further preclinical development of Mn-based nano-medication for anti-ROS mediated inflammatory disease therapy.

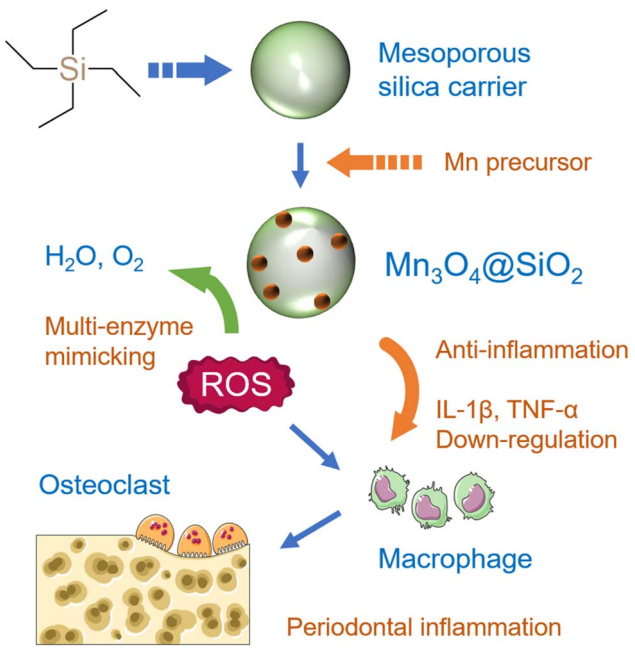

Scheme 1 Illustration of the preparation and anti-gingivitis application of the Mn_3O_4@SiO_2 NPs.

2. Materials and methods

2.1. Materials and instrumentation

Tetraethyl orthosilicate (TEOS), triethanolamine (TEA), hexadecyltrimethylammonium chloride (CTAC), manganese acetate, salicylic acid (SA), anhydrous ethanol, $FeSO_4$, and H_2O_2 (30 wt%) were purchased from Aladdin Scientific Corp. (Shanghai, China). 4% paraformaldehyde, phorbol 12-myristate 13-acetate (PMA), 2′,7′-dichlorofluorescein diacetate (DCFH-DA) were supplied by Macklin Co., Ltd (Shanghai, China). All chemical reagents were used as received without any further purification. All aqueous solutions were prepared with deionized water (18.2 MΩ cm, Millipore).

Dulbecco's Modified Eagle's Medium (DMEM), phosphate-buffered saline (PBS), and fetal bovine serum (FBS) were purchased from ThermoFisher Scientific Shanghai Branch (Shanghai, China). Total Superoxide Dismutase Assay Kit (WST-1, Cat. No. C0035), Catalase Assay Kit (Cat. No. S0038), Cell Counting Kit-8 (CCK-8, Cat. No. C0037), Mouse IL-1β ELISA Kit (Cat. No. PI301), and Mouse TNF-α ELISA Kit (Cat. No. PT512) were purchased from Beyotime Biotechnology (Shanghai, China). The cell lines, including RAW 264.7, were obtained from Cellcook Ltd (Guangzhou, China). Male ICR mice (SPF grade) were acquired from GemPharmatech Co., Ltd (Nanjing, China).

In terms of instrumentations, transmission electron microscopy (TEM) images were obtained using a JEM-1400 electron microscope (JEOL, Japan), element mapping images were recorded by a JEM-F200 electronic microscope (JEOL, Japan) equipped with energy dispersive spectroscopy (EDS), and the samples were prepared on a copper mesh with 200-mesh carbon support film and the used voltage was 120 kV. Dynamic light scattering (DLS) and zeta-potential data were collected using a Litesizer 500 scatterometer (Anton Paar, Austria). Powder X-ray diffraction (XRD) data were collected with a Rigaku Ultima diffractometer using Cu Kα radiation. The diffractometer was operated at 40 kV and 40 mA with a scan rate of 5° min^{-1}. The specific surface area was measured at 77 K using a Kubo X1000 (Biaode, China). The concentration of elemental Mn was determined using an Avio 220 Max inductively coupled plasma optical emission spectrometer (ICP-OES, PerkinElmer, USA), and the samples were prepared using an M3 microwave digestion system (PreeKem, China). Ultraviolet-visible (UV-vis) absorption spectra were recorded on a UV3600 spectrometer (Shimadzu, Japan). Fluorescence spectra were obtained using an LS-55 spectrometer (PerkinElmer, USA). Fluorescence images were captured on an FV3000 confocal laser scanning microscope (CLSM, Olympus, Japan). The *in vivo* fluorescence imaging of the live mice was conducted on a PerkinElmer *in vivo* imaging system (PerkinElmer, USA) with an excitation wavelength of 465 nm and an emission wavelength of 520 nm.

2.2. Preparation of the Mn_3O_4@SiO_2 NPs

The chemical synthesis of the Mn_3O_4@SiO_2 NPs was conducted by following a method described in the literature.[30] Typically, 1.0 g of CTAC was dissolved together with 0.01 g of TEA in 10 mL

of deionized water at 95 °C under magnetic stirring. After 1 h, 0.8 mL of TEOS was added dropwise under continuous stirring and kept for another 1 h. The resultant SiO_2 NPs were collected by centrifugation at 4000 rpm for 15 min and washed several times with ethanol.

The Mn_3O_4 NPs were synthesized by following a previous literature report.[19] In a typical procedure, 0.6 g of manganese acetate was dissolved in 30 mL of anhydrous ethanol and magnetically stirred until fully dissolved. The mixture was transferred into a 50 mL Teflon-lined stainless-steel autoclave for thermal treatment at 120 °C. After 24 h, the resultant Mn_3O_4 NPs were washed with deionized water three times.

1.0 g of the SiO_2 NPs prepared above were dispersed in 30 mL of anhydrous ethanol containing 0.5 g of manganese acetate; the mixture was transferred into a 50 mL Teflon-lined stainless-steel autoclave for thermal treatment at 120 °C. After 24 h, the resultant Mn_3O_4@SiO_2 NPs were collected by centrifugation at 4000 rpm for 15 min and washed with deionized water three times for further characterization.

2.3. Multi-enzymatic ROS scavenging assay

The SOD- and CAT-like catalytic activities of the Mn_3O_4@SiO_2 NPs were evaluated with a Total Superoxide Dismutase Assay Kit, and a Catalase Assay Kit, respectively, according to the protocol from the manufacturer, using the equal stoichiometric Mn_3O_4 NPs as a comparison.

The $^{\bullet}OH$ eliminating capacity of the Mn_3O_4@SiO_2 NPs as well as the Mn_3O_4 NPs was determined by measuring the characteristic absorbance of dihydroxybenzoic acid at 510 nm, which was produced when SA reacted with $^{\bullet}OH$, as shown in Fig. 2D. Typically, the $^{\bullet}OH$ radicals were generated through the Fenton reaction of 1.8 mM $FeSO_4$ and 5 mM H_2O_2 for 10 min at room temperature. The NPs at various concentrations were incubated with the Fenton system mentioned above, and 1.8 mM of SA was added after 2 min. The absorbance of dihydroxybenzoic acid was recorded using the UV-vis spectrometer at room temperature with a 1 cm quartz cuvette.

2.4. *In vitro* biocompatibility and intracellular ROS scavenging

The cytotoxicity of the NPs was evaluated against RAW 264.7 cell lines, which were refreshed and seeded in 96-well plates at a density of 5000 cells per well in DMEM (supplemented with 10% FBS and 1% penicillin-streptomycin) at 37 °C and under a 5% CO_2 atmosphere for 24 hours. The culture medium was then replaced with 100 μL DMEM dispersions containing the NPs at doses of 1, 5, 10, 20 mg L^{-1} (calculated based on the mass of Mn_3O_4), with 5 duplicated wells and incubated for a further 24 hours. Cell viability was then determined using the CCK-8 assay according to the protocol provided by the manufacturers.

In 20 mm confocal Petri dishes, 10^3 cells per well of RAW 264.7 cells were inoculated and incubated with 10 μL of H_2O_2 (10 mM) at 37 °C and 5% CO_2 atmosphere for 24 hours. Thereafter, the medium was withdrawn for further ELISA (enzyme-linked immunosorbent assay) analysis following the protocol provided by the manufacturer, and substituted with 1 mL of medium containing 10 μg of the Mn_3O_4@SiO_2 NPs and the Mn_3O_4 NPs, respectively, and the dish was left to incubate for a further 24 hours. Subsequently, 0.1 mL of DCFH-DA (0.01 mM) in a serum-free medium without phenol red was added to each dish, and the staining process was conducted in the dark for a duration of 30 minutes. Next, fixation with 1 mL of 4% paraformaldehyde was performed for 15 minutes, followed by washing with PBS, before the cells were observed using CLSM.

2.5. *In vivo* anti-inflammation therapy

The animal experiments of this study have been approved by the Science and Technology Ethics Committee of Nanjing University (Approval No. IACUC-2412013), ensuring adherence to ethical standards. Firstly, 12 male ICR mice were randomly divided into 4 groups with 3 mice per group. 5 μL of PMA (1 mg mL^{-1}) was topically applied on the alveolar mucosa of the buccal side in the mandible of each mouse from 3 groups to induce the acute gingivitis model, leaving one group as the control. After 6 h of induction, the mice from the experimental groups were anesthetized and injected with 5 μL saline within the inflamed focus established before, containing the Mn_3O_4@SiO_2 NPs or the Mn_3O_4 NPs (at a dose of 1.0 μg kg^{-1} bodyweight, calculated based on the content of Mn_3O_4). After 0.5 h of incubation, 5 μL of DCFH-DA (1 mM) was injected in a similar way. After another 0.5 h, the *in vivo* fluorescence images were recorded using a PerkinElmer *in vivo* imaging system with an excitation wavelength of 465 nm and an emission wavelength of 520 nm.

The mice were sacrificed and dissected afterward, with the vital tissues of the gingiva collected and fixed in 4% paraformaldehyde, and subsequently embedded in paraffin. 4 μm sections were prepared and stained with hematoxylin and eosin (H&E), and observed using a digital pathological microscope.

For *in vivo* cytokines assay, the gingivitis mouse model was established and treated again with 5 mice per group, following the identical protocol described above, and the gingiva tissues from the buccal palate were collected 6 h after administration and homogenized with 0.01 M PBS for TNF-α and IL-1β evaluations using ELISA kits following the protocol provided by the manufacturer.

2.6. *In vivo* biocompatibility evaluation

In terms of the biosafety study, 3 mice per group were subgingiva injected with the Mn_3O_4@SiO_2 or the Mn_3O_4 NPs at a dose of 10 μg kg^{-1} bodyweight, calculated based on the content of Mn_3O_4, and sacrificed at the designated time after administration. Blood and tissue from the liver and kidneys were collected for Mn content quantification *via* ICP-OES. Other groups were sacrificed 7 days after administration, with the collection of the heart, liver, spleen, kidney, and lung for H&E staining and observation.

2.7. Statistical analysis

All data are expressed as mean ± standard deviation (SD). Two-group comparisons were conducted using a two-tailed unpaired Student's *t*-test to examine the statistical differences using the

GraphPad Prism 8.0 software. Statistical significance was considered as $p < 0.05$.

3. Results and discussion

3.1. Preparation and characterization of the Mn_3O_4@SiO_2 nanoparticles

Firstly, the Mn_3O_4 NPs were synthesized by following a hydrothermal method from the literature, and the TEM technique was employed to analyze the morphology and the phase composition of the as-prepared Mn_3O_4 NPs. From Fig. 1A, it can be seen that the morphology of the Mn_3O_4 NPs was nearly spherical, and the aggregation of the Mn_3O_4 NPs could also be observed in a large area in the field of vision. The size distribution of the Mn_3O_4 NPs ranged from 4 nm to 10 nm according to the DLS analysis shown in Fig. 1D. The mesoporous SiO_2 NPs were subsequently synthesized by following a surfactant-assisted template method from the literature,[30] and the morphology and particle size distribution (polydispersity index, PDI) of the as-synthesized SiO_2 NPs are demonstrated in Fig. 1B, D and Table 1. The SiO_2 NPs were spherical in shape and ranged in size from 100 nm to 120 nm.

Based on the nano-materials and their preparation protocols above, the Mn_3O_4 NPs were *in situ* synthesized using the SiO_2 NPs as a template. As demonstrated in Fig. 1C, the sub-10 nm Mn_3O_4 NPs were mostly located in the outer shell of the 100 nm sized SiO_2 NPs, and no obvious change in hydrodynamic size was observed between the as-prepared Mn_3O_4@SiO_2 NPs and

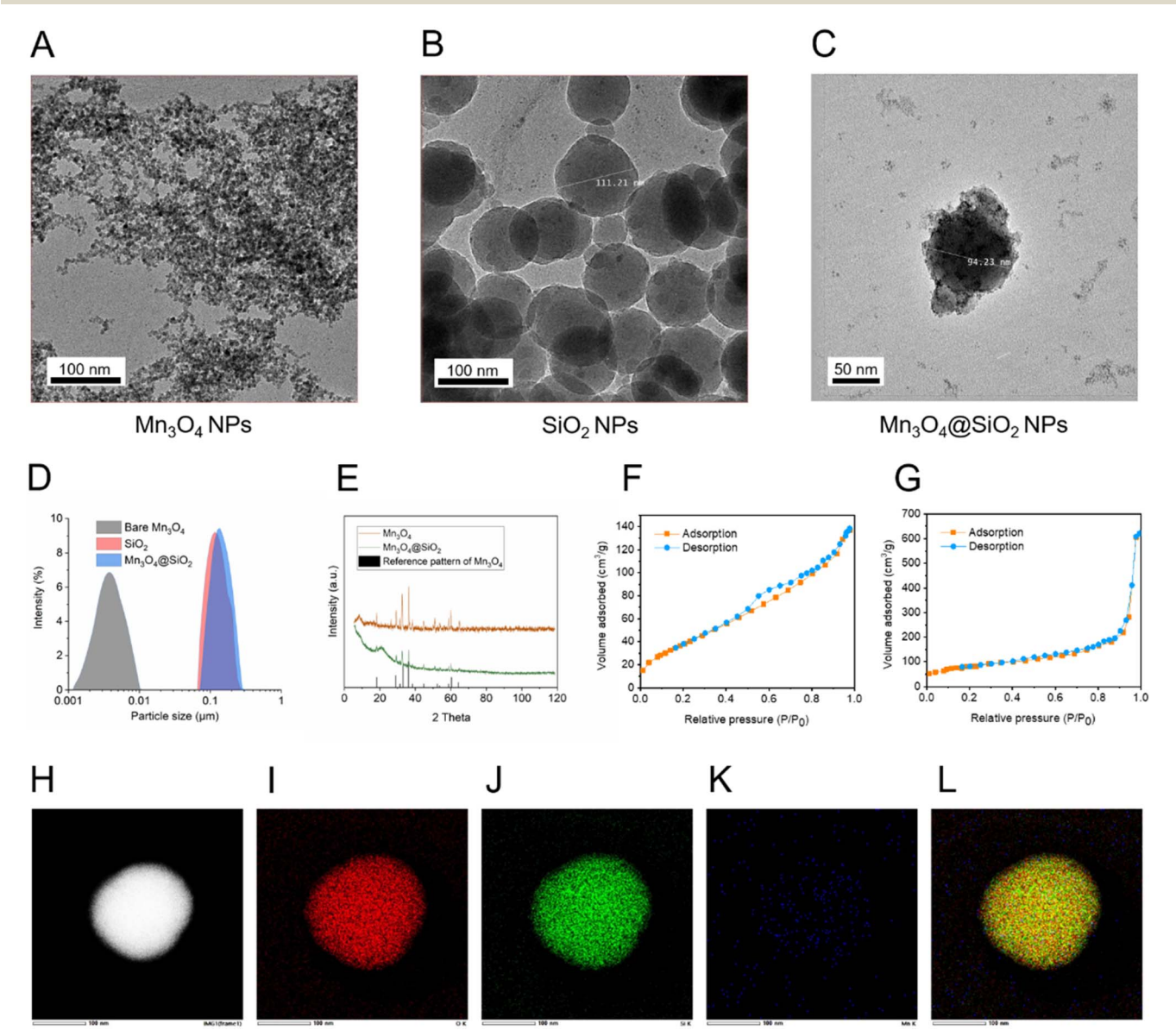

Fig. 1 Characterization of the Mn_3O_4@SiO_2 NPs and their precursors. (A)–(C) TEM images of the indicated NPs; (D) hydrodynamic diameters of the indicated NPs (10 μg mL^{-1} in PBS); (E) XRD patterns of the indicated NPs; (F) and (G) nitrogen adsorption–desorption curves of the SiO_2 and Mn_3O_4@SiO_2 NPs; and (H)–(L) EDS mapping images of the Mn_3O_4@SiO_2 NPs ((H) TEM image, (I–K). O, Si, Mn element mapping images, respectively, and (L) merged image).

Table 1 Physical properties of the indicated NPs

Sample	Diameter (DLS, nm)	PDI	Zeta-potential (mV)	Surface area (m^2 g^{-1})
SiO_2	114.5 ± 5.2	0.219	−43.3 ± 2.3	316.2 ± 7.9
Mn_3O_4@SiO_2	105.7 ± 1.4	0.176	−27.5 ± 1.8	198.2 ± 4.3

their precursor SiO_2 NPs, according to Fig. 1D. The XRD patterns of the bare Mn_3O_4 NPs and the Mn_3O_4@SiO_2 NPs are shown in Fig. 1E, from which it can be seen that the measured diffraction peaks matched well to the standard pattern of hausmannite Mn_3O_4 [JCPDS card No. 24-0734], confirming their highly crystalline nature and the identity of the resulting NPs. The content of the Mn element was found to be 18.35 ± 0.05 wt% of the Mn_3O_4@SiO_2 NPs by ICP-OES analysis, and the Mn_3O_4 loading content of the Mn_3O_4@SiO_2 NPs was calculated to be 25.47 ± 0.07 wt%.

The mesoporous nature of the SiO_2 NPs (Fig. 1F) and the Mn_3O_4@SiO_2 NPs (Fig. 1G) was verified with isothermal nitrogen adsorption–desorption and calculated using the Brunauer–Emmett–Teller (BET) method. The typical curve of a hysteresis loop observed in Fig. 1F and G indicated that the SiO_2 NPs with mesoporous structure provided plenty of space for *in situ* growth of the Mn_3O_4 NPs, resulting in Mn_3O_4@SiO_2 NPs with reduced specific surface area (Table 1) that was partially occupied by the Mn_3O_4 NPs.

To further confirm the existence and distribution of the Mn_3O_4 incorporated into the SiO_2 NPs, the EDS mapping of the as-prepared Mn_3O_4@SiO_2 NPs was investigated, and the results are shown in Fig. 1H–L. From Fig. 1H, it could be observed that a single nanoparticle of the Mn_3O_4@SiO_2 NPs with a diameter of about 100 nm was spherical and in accordance with Fig. 1C. The distribution of the O, Si, and Mn elements was clearly visualized in Fig. 1I–K, respectively, and shows that the Mn (blue dots in Fig. 1K) was uniformly distributed in the SiO_2 NPs. Combined with the crystalline nature of the Mn_3O_4 supported in Fig. 1E, and the merged element distribution in Fig. 1L, the results above indicate that the Mn_3O_4@SiO_2 NPs with Mn_3O_4 NPs separately scattered on them were successfully synthesized.

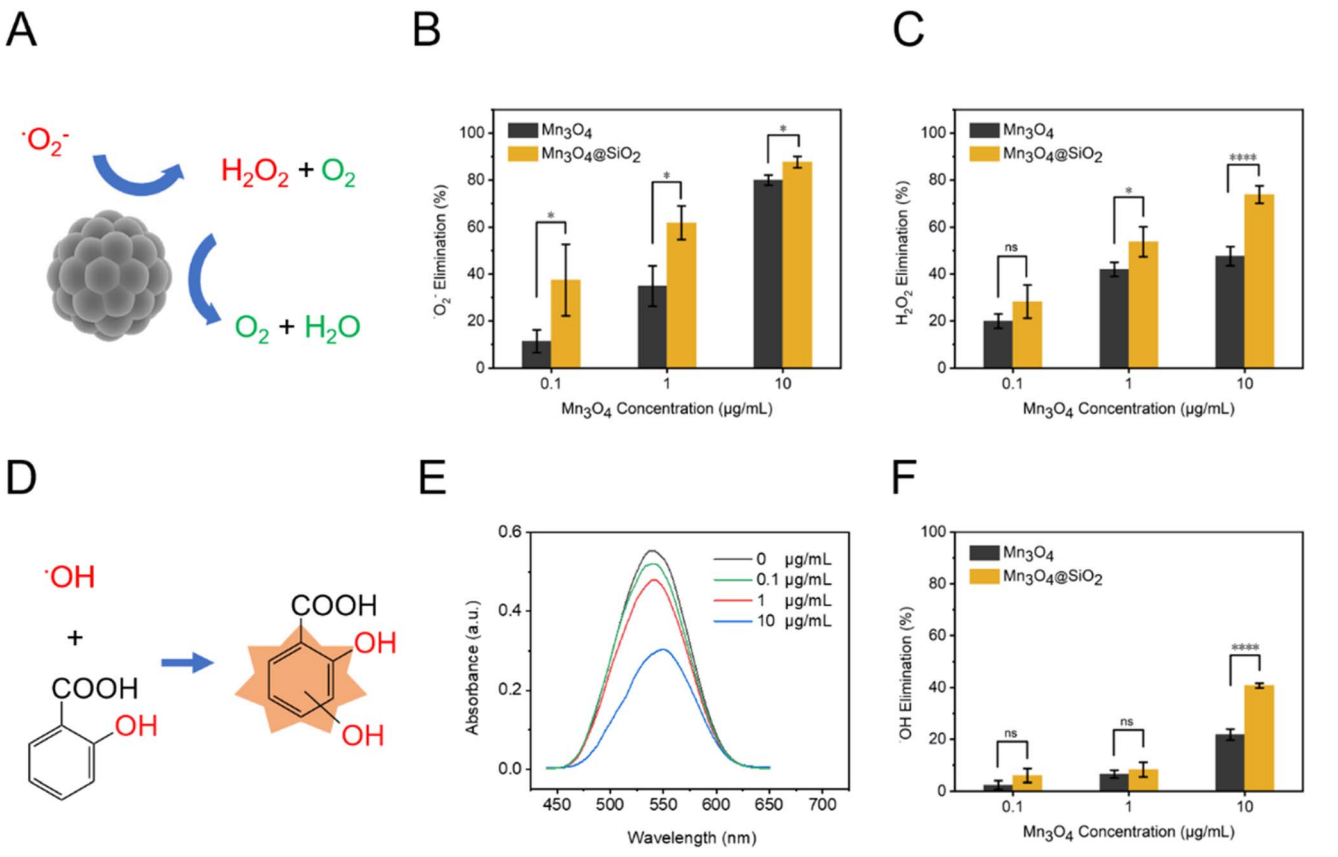

Fig. 2 The multi-enzyme mimic activities of the Mn_3O_4@SiO_2 NPs and the Mn_3O_4 NPs at the same concentration of Mn_3O_4. (A) Integrated SOD and CAT mimetic activity of the Mn_3O_4@ SiO_2 NPs; (B) and (C) $^{\cdot}O_2^-$ and H_2O_2 scavenging capacities of the indicated NPs, respectively; (D) illustration of the determination of $^{\cdot}OH$ reaction with SA using fluorescence detection; (E) typical fluorescence spectra of the resultant of SA and $^{\cdot}OH$ cultured with various concentrations of the Mn_3O_4@ SiO_2 NPs; and (F) $^{\cdot}OH$ scavenging assay of the indicated materials. *p < 0.05, ****p < 0.001, ns = not significant. The data in the histogram are shown as means ± SD (n = 5).

3.2. Multi-enzymatic ROS scavenging assay

To examine the biocatalytic activities of the Mn_3O_4@SiO_2 NPs prepared above, the elimination of $^{\bullet}O_2^-$ and H_2O_2 was evaluated using the WST-1 and H_2O_2 assay kits, respectively. As shown in Fig. 2B and C, dose-dependent $^{\bullet}O_2^-$ and H_2O_2 removal could be observed for the Mn_3O_4@SiO_2 NPs, indicating that the Mn_3O_4@SiO_2 NPs possess both SOD-like and CAT-like enzyme-mimic catalytic activities, as schematically illustrated in Fig. 1A. It should be noted that the Mn_3O_4@SiO_2 NPs quenched over 60% of the $^{\bullet}O_2^-$ at a Mn_3O_4 concentration of 1 μg mL^{-1}, which was about 2 times the efficiency of the Mn_3O_4 NPs at the same concentration. The $^{\bullet}O_2^-$ and H_2O_2 scavenging efficacies of the Mn_3O_4@SiO_2 NPs were superior to those of the Mn_3O_4 NPs at equal concentrations of Mn_3O_4.

The $^{\bullet}OH$ radical is considered to be one of the most aggressive ROS, which causes oxidative stress by attacking proteins and DNA and thus leading to damage of cells and tissues. However, to the best of our knowledge, there is no natural enzyme identified that specifically tackles $^{\bullet}OH$. As a matter of fact, therapeutic agents with $^{\bullet}OH$ scavenging capacity are of great importance for anti-inflammation biomedical applications. The $^{\bullet}OH$ scavenging capacity of the Mn_3O_4@SiO_2 NPs was thus assessed by utilizing SA as the specific probe, and this was quantitatively analyzed with UV-vis absorption, as shown in Fig. 2D. The representative UV-vis spectra of various concentrations of the Mn_3O_4@SiO_2 NPs upon encountering $^{\bullet}OH$ radicals, generated by the Fenton reaction with the Fe^{2+}/H_2O_2 system, are shown in Fig. 2E. An obvious absorption peak at 540 nm is observed, which is attributed to the result of SA reacting with the $^{\bullet}OH$. The absorption intensities of the indicated concentrations revealed a dose-dependent decrease with the addition of the Mn_3O_4@SiO_2 NPs, which exhibit a higher $^{\bullet}OH$ eliminating efficiency compared with an equal stoichiometry of the Mn_3O_4 NPs.

All these results indicated the effectiveness of the Mn_3O_4@SiO_2 NPs for multiple ROS elimination and their potential for use in biomedical applications in the treatment of ROS-associated diseases. This treatment capacity could be attributed to the enhanced dispersity of the Mn_3O_4 NPs on the SiO_2 NPs.

3.3. *In vitro* cytotoxicity and ROS-scavenging capacity of the Mn_3O_4@SiO_2 NPs

Cytotoxicity experiments were conducted to evaluate the effect of the Mn_3O_4@SiO_2 NPs on cell viability. As a crucial intermediator that stimulates and modulates the inflammatory process, a macrophage (murine RAW 264.7) was selected to evaluate the biocompatibility of the Mn_3O_4@SiO_2 NPs. As

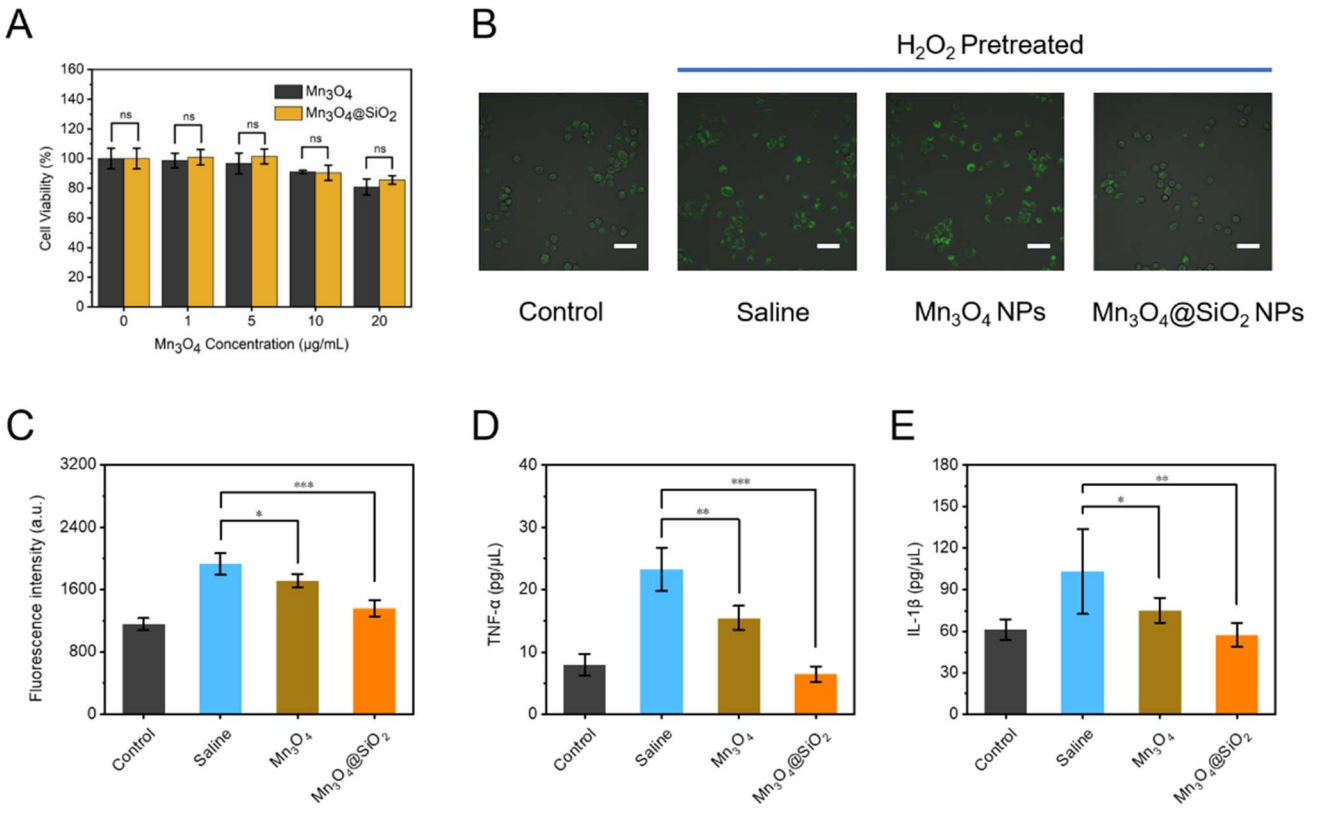

Fig. 3 The *in vitro* anti-ROS effects and biocompatibility of the NPs. (A) Cytotoxicity of the NPs against RAW 264.7 cells; (B) intracellular ROS imaging of RAW 264.7 cells pretreated with 10 mM H_2O_2 co-cultured with 10 μg mL^{-1} of the indicated materials (for all groups, the gain value was 720, laser intensity was 7.28%, and exposure time was 20 ms); (C) corresponding fluorescence intensity of (B); and (D) and (E) TNF-α and IL-β concentrations of the culture medium of RAW 264.7 cells incubated with 10 μg mL^{-1} of the indicated materials, respectively. *p < 0.05, **p < 0.01, ***p < 0.005, ns = not significant. The data in the histogram are shown as means ± SD (n = 5).

shown in Fig. 3A, the Mn_3O_4@SiO_2 NPs as well as the Mn_3O_4 NPs exhibited no obvious cytotoxicity toward RAW 264.7 cells when the Mn_3O_4 concentration was below 5 μg mL^{-1}. The cytotoxicity of the Mn_3O_4@SiO_2 NPs was above 90% when their concentration increased to 20 μg mL^{-1}.

The RAW 264.7 cells were again co-cultured with the Mn_3O_4@SiO_2 NPs to further explore their *in vitro* ROS-scavenging activity, by visualizing ROS with DCFH-DA as the intracellular fluorescent probe. The probe was inactivated in a non-fluorescent state and could penetrate the cells to then be hydrolyzed by enzymes in the living cells into DCFH, which was then oxidized by the ROS to yield the fluorescent molecule 2′,7′-dichlorofluorescein (DCF). As shown in Fig. 3B, the fluorescence intensity inside the RAW 264.7 cells stimulated with 10 mM H_2O_2 was greatly enhanced compared to that of the control group, indicating the severity of the oxidative stress, which was partially relieved with co-cultured Mn_3O_4 NPs with a decreased fluorescence. In contrast, *in vitro* inflammation of RAW 264.7 cells was remarkably attenuated by the treatment with the Mn_3O_4@SiO_2 NPs. To clearly visualize the morphology of the cells in the control group (low ROS content and weak fluorescence), the fluorescence signal of the FITC channel (wavelength of 520 nm) of the CLSM was amplified to 7.28% (laser intensity) by adjusting the software. This setting was applied to all groups under the same parameters throughout the experiment for comparative observation. The quantitative comparison is summarized in Fig. 3C and indicates that the Mn_3O_4@SiO_2 NPs possessed superior intracellular ROS-scavenging capacity over the Mn_3O_4 NPs at the same concentration of Mn_3O_4.

To further explore the *in vitro* anti-inflammation efficacy of the Mn_3O_4@SiO_2 NPs, two representative pro-inflammation cytokines, TNF-α and IL-1β, in the culture medium of the RAW 264.7 cells were both quantitatively analyzed with relative ELISA kits. Fig. 3D and E show a similar tendency for both TNF-α and IL-1β that was identical with the variation in the ROS shown in Fig. 3B, thus indicating that the principal pro-inflammation cytokines TNF-α and IL-1β could be discernibly sequestrated by the Mn_3O_4@SiO_2 NPs in cultured cells experiencing ROS-related oxidative stress. The anti-oxidant and anti-inflammatory effects of the Mn_3O_4@SiO_2 NPs were thoroughly investigated by conducting the *in vitro* evaluations above, which demonstrated that the Mn_3O_4@SiO_2 NPs with mesoporous structure, enlarged and isolated catalytical sites, possessed multi-enzyme mimicking capacity for efficient ROS scavenging efficacy, thus demonstrating their potential for application in anti-inflammation therapy.

3.4. *In vivo* anti-inflammation therapy

Encouraged by the *in vitro* multi-enzyme mimic ROS scavenging activities and pro-inflammation cytokine suppressing capacity

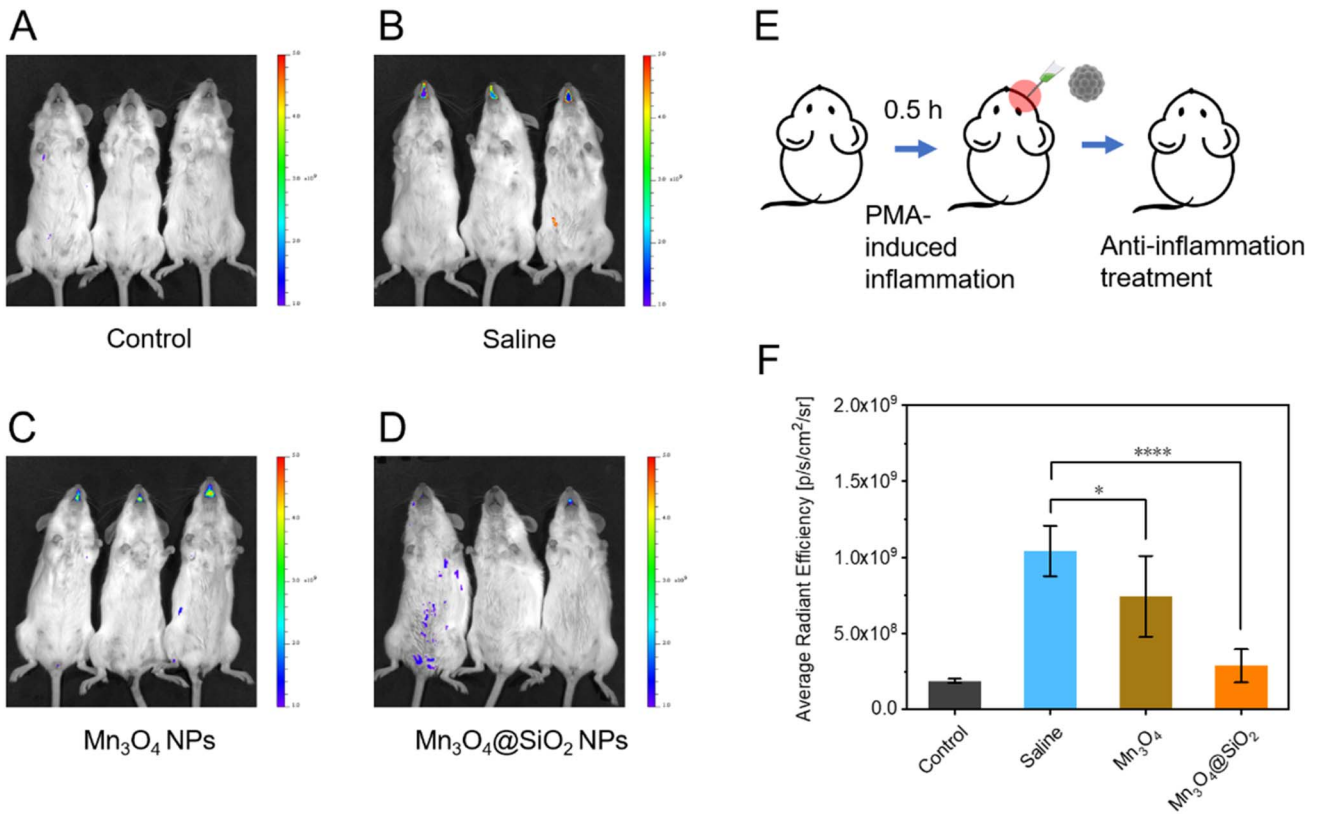

Fig. 4 The results of the *in vivo* anti-inflammation therapy. (A)–(D) The whole-body *in vivo* fluorescence images of mice from the indicated groups, the pseudo-color scale next to the image indicates radiant efficiency (p per s per cm^2 per sr); (E) illustration of the workflow for obtaining the acute gingivitis mouse model; and (F) the fluorescence intensity of the inflamed areas in (A)–(D). *$p < 0.05$, ****$p < 0.001$. The data in the histogram are shown as means ± SD ($n = 3$).

of the Mn_3O_4@SiO_2 NPs verified above, the *in vivo* anti-inflammation efficacy of the Mn_3O_4@SiO_2 NPs was investigated by establishing an acute-gingivitis mouse model, as described in Fig. 4E. To this end, the gingivae of the ICR mice were subjected to PMA, a protein kinase C (PKC) activator that stimulates acute inflammation and subsequent onset of acute gingivitis, thus resulting in red and swollen gums 6 h after treatment with PMA. The inflammation correlated ROS were again visualized and studied with DCFH-DA as the *in vivo* fluorescence dye, and yielded a strong fluorescence signal around the gums of the mice in the PMA-induced gingivitis model groups treated with saline (Fig. 4B) and the Mn_3O_4 NPs (Fig. 4C) when compared to the control group (Fig. 4A).

In contrast, the Mn_3O_4@SiO_2 NPs remarkably reduced the fluorescence intensity (Fig. 4D) at the same dosage (calculated based on the mass of Mn_3O_4) as the group that was treated with the Mn_3O_4 NPs. The statistical results are summarized in Fig. 4F, which indicates that an over 5-fold increase in fluorescence intensity was evoked by the PMA-induced gingivitis compared to that of the control group, and about 70% of the total ROS in the inflamed gums could be scavenged by the Mn_3O_4 NPs. As shown in Fig. 4F, the Mn_3O_4@SiO_2 NPs exhibited tremendous anti-oxidant activity, over 2 times to that of the Mn_3O_4 NPs at the same concentration of Mn_3O_4, which is partially attributed to the anti-aggregation ability and catalytic area enlargement of the mesoporous nano-SiO_2 supported Mn_3O_4 NPs.

After examination of the *in vivo* anti-ROS efficacy, the PMA-induced gingivitis mouse model was established again with 5 mice per group, following the identical protocol used in the *in vivo* fluorescence imaging. The buccal tissues from the palate of the mice were collected 6 h after treatment with the NPs or saline for comparison, and they were stained with H&E for subsequent pathological observation (Fig. 5A–D), or homogenized for ELISA study of the levels of TNF-α (Fig. 5E) and IL-1β (Fig. 5F). As shown in Fig. 5B, the tissue was sabotaged by the PMA-induced acute inflammation, manifesting in derangement of the tissue and infiltration of the inflammatory immune cells (red arrow). This was partially compromised with the treatment of the Mn_3O_4 NPs (Fig. 5C), but effectively rescued by the Mn_3O_4@SiO_2 NPs at the same concentration of Mn_3O_4. After confirmation of the superior *in vivo* anti-inflammation efficacy with pathological observation, the levels of the principal inflammatory cytokines including TNF-α and IL-1β were further quantified, as shown in Fig. 5E and F, respectively. From the quantification of the key cytokines during inflammation, it could be observed that the expression of TNF-α was severely suppressed by the Mn_3O_4@SiO_2 NPs with a 4-fold decreased

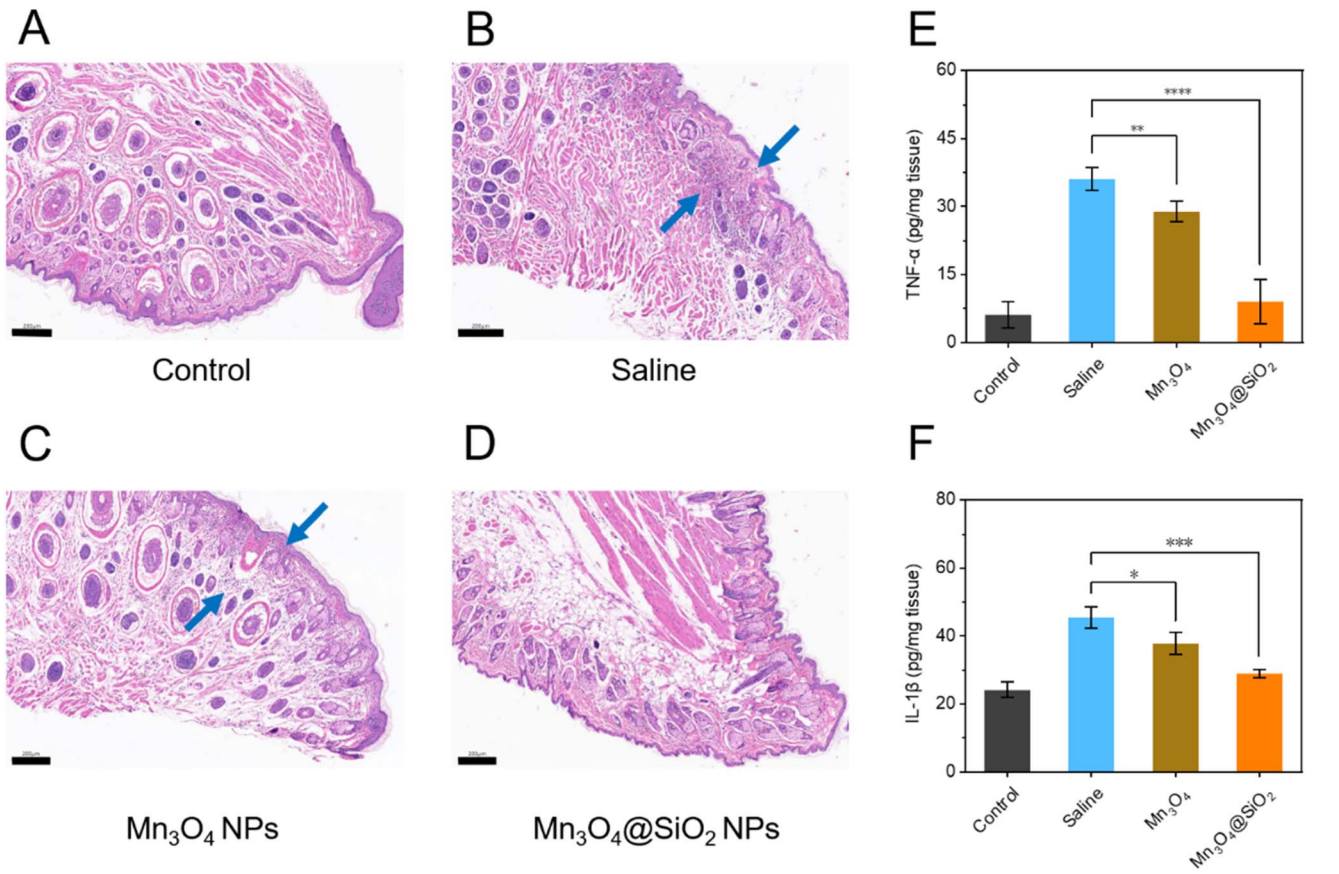

Fig. 5 The *in vivo* therapeutic efficacy in a gingivitis mouse model. (A)–(D) H&E-stained tissues from the buccal palate (bar = 200 μm, the blue arrows indicate inflammatory infiltration); and (E) and (F) TNF-α and IL-1β levels from the buccal palate homogenates of the indicated groups, respectively. *p < 0.05, **p < 0.01, ***p < 0.005, ****p < 0.001. The data in the histogram are shown as means ± SD (n = 5).

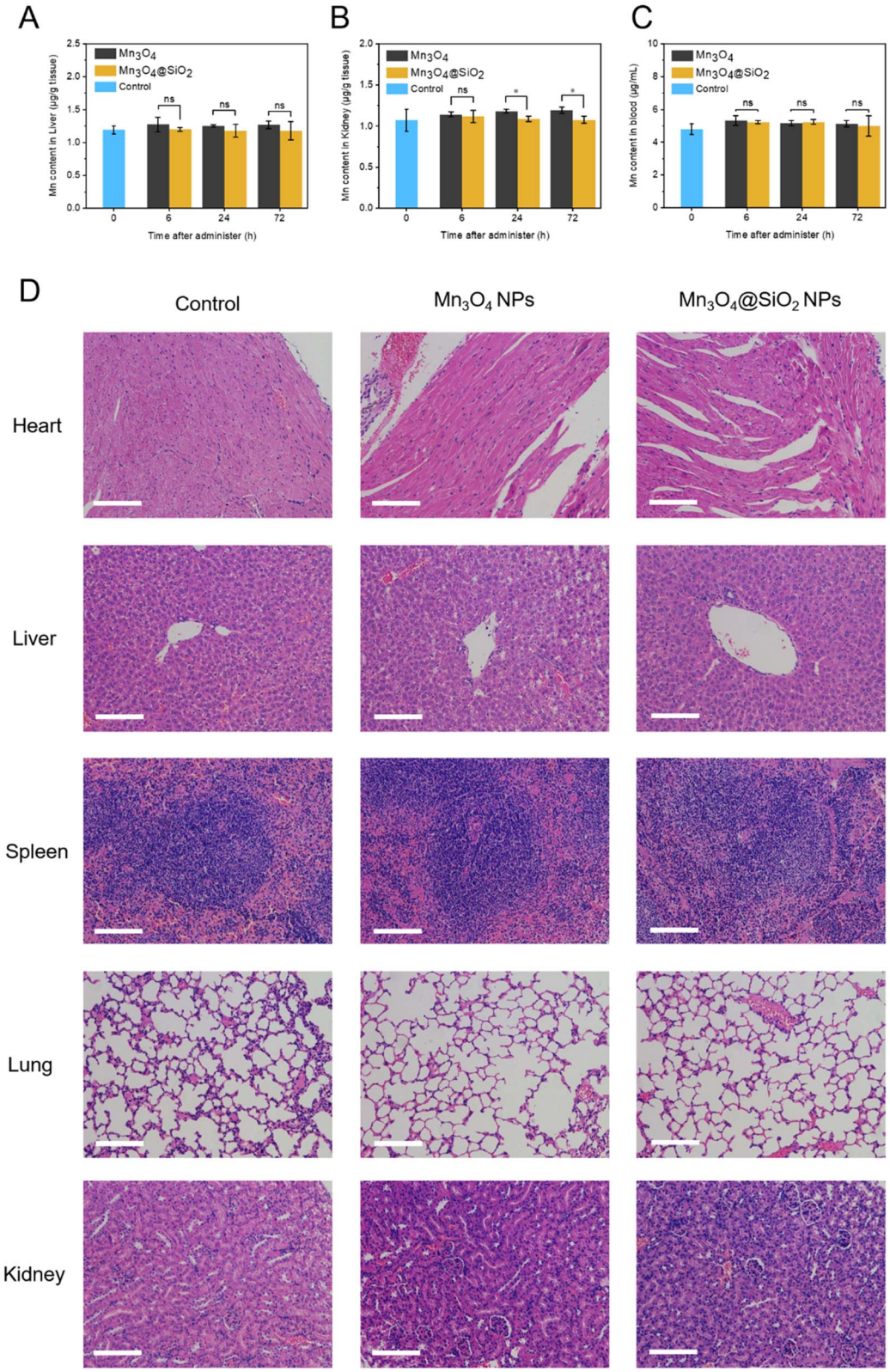

Fig. 6 *In vivo* biocompatibility evaluation for the Mn_3O_4@SiO_2 NPs. (A)–(C) Mn content in liver, kidney and blood of the indicated NPs at different times after intra-gingiva administration, respectively; and (D) H&E-stained tissues 7 days after intra-gingiva administration of the indicated NPs (bar = 200 μm). *$p < 0.05$, ns, not significant. The data in the histogram are shown as means ± SD ($n = 3$).

compared with the untreated group and 3 times the efficacy of the Mn_3O_4 NPs-treated group. The Mn_3O_4@SiO_2 NPs also exhibited higher effectiveness toward IL-1β down-regulation over the Mn_3O_4 NPs at the same dosage of Mn_3O_4, which together verified the effective *in vivo* inflammatory cytokine sequestration efficacy of the Mn_3O_4@SiO_2 NPs.

3.5. *In vivo* biocompatibility evaluation

Based on the premise of ensuring *in vitro* safety, the interference of *in vivo* Mn metabolism caused by the Mn_3O_4@SiO_2 NPs was investigated by chronological quantification of the Mn in the liver, kidney, and blood using ICP-OES, as shown in Fig. 6A–C, respectively. As demonstrated in Fig. 6A and C, the Mn content in the liver and blood from the mice that received the Mn_3O_4@SiO_2 NPs or the Mn_3O_4 NPs at a dosage of 10 μg kg^{-1} bodyweight (calculated based on the content of Mn_3O_4), which was 10 times that of the anti-gingivitis therapy (1 μg kg^{-1}), was not obviously increased compared with the control group, and the groups administered either of the NPs did not show significant differences within the experimental period. The Mn content in the kidney (Fig. 6B) showed an identical tendency compared with that from Fig. 6A and C within 6 h after administration. The mice that received the Mn_3O_4@SiO_2 NPs exhibited steady Mn content in the kidney, while an equal dosage of the Mn_3O_4 NPs exerted a non-negligible increase in the Mn content in the kidney. The results above indicated that the bare Mn_3O_4 NPs were prone to rapid degradation after administration, which therefore enhanced their potential toxicity to the kidney. In contrast, the encapsulation of the Mn_3O_4 within the mesoporous SiO_2 NPs provided a separated niche that protected it from *in vivo* decomposition, which not only inhibited the accumulation of Mn in the kidney by degradation resistance but also remarkably reduced the therapeutic dosage of Mn_3O_4 NPs required *via* enlargement of the catalytic area of the multi-enzyme mimicking Mn_3O_4@SiO_2 NPs.

To further study the latent *in vivo* toxicity or delayed immune response evoked by the Mn_3O_4@SiO_2 NPs, histological analysis of H&E-stained sections from the main organs, including the heart, liver, spleen, lungs, and kidneys of the mice that received the Mn_3O_4@SiO_2 NPs at a dosage of 10 μg kg^{-1}, was conducted and is summarized in Fig. 6D. Pathological examination revealed no discernible lesions to the listed organs 7 days after administration, suggesting that the Mn_3O_4@SiO_2 NPs did not initiate significant *in vivo* toxicity at a dosage 10 times higher than the effective anti-inflammatory therapeutic dosage.

4. Conclusions

In summary, sub-10 nm sized Mn_3O_4 NPs grown *in situ* and arranged in the mesoporous SiO_2 NPs with diameters of about 100 nm were successfully prepared and verified with comprehensive characterization. The Mn_3O_4@SiO_2 NPs exhibited a remarkable scavenging capacity of various ROS by mimicking multiple anti-oxidant enzymes. Satisfactory cellular protection from oxidative stress and *in vitro* biosafety were observed in the Mn_3O_4@SiO_2 NPs co-cultured cells. Furthermore, the *in vivo* anti-inflammation experiments indicated that the Mn_3O_4@SiO_2 NPs effectively relieved inflammation in an acute gingivitis mouse model by scavenging ROS and subsequently sequestrating inflammatory cytokines. *In vivo* biosafety exploration revealed no overt abnormalities in major organs over 7 days after administration of the Mn_3O_4@SiO_2 NPs, and Mn content in the liver, kidney and blood was steady and not obviously increased during a period of 72 h. The aforementioned Mn_3O_4@SiO_2 NPs are an anti-inflammation nano-agent with enhanced therapeutic capacity that reduces systemic toxicity and could serve as a potentially valuable medication for biomedical applications for gingivitis and other ROS-related inflammation management.

Conflicts of interest

The authors declare no conflicts of interest.

Data availability

The authors confirm that the data supporting the findings of this study are available within the article.

Acknowledgements

The authors gratefully acknowledge support for this research from the Key Natural Science Research Project of Universities in Anhui Province (Grant Number 2023AH051741) and the Program for Excellent Sci-tech Innovation Teams of Universities in Anhui Province (Grant/Award Number: 2023AH010073).

References

1 F. A. Scannapieco and A. Cantos, *Periodontology*, 2000, **2016**(72), 153–175.
2 D. F. Kinane, P. G. Stathopoulou and P. N. Papapanou, *Nat. Rev. Dis. Primers*, 2017, **3**, 17039.
3 G. Hajishengallis, *Nat. Rev. Immunol.*, 2015, **15**, 30–44.
4 T. Kwon, I. B. Lamster and L. Levin, *Int. Dent. J.*, 2021, **71**, 462–476.
5 P. M. Preshaw, *Periodontology*, 2000, **2018**(76), 131–149.
6 P. M. Bartold and T. E. Van Dyke, *Periodontology*, 2000, **2017**(75), 317–329.
7 F. P. Deus and A. Ouanounou, *Int. Dent. J.*, 2022, **72**, 269–277.
8 Y. Xi, Y. Wang, J. Gao, Y. Xiao and J. Du, *ACS Nano*, 2019, **13**, 13645–13657.
9 A. Cekici, A. Kantarci, H. Hasturk and T. E. Van Dyke, *Periodontology*, 2000, **2014**(64), 57–80.
10 W. Pan, Q. Wang and Q. Chen, *Int. J. Oral Sci.*, 2019, **11**, 30.
11 R. A. Floyd and J. M. Carney, *Ann. Neurol.*, 1992, **32**, S22–S27.
12 X. Ren, Z. Huang, M. Han, Y. Meng, H. Li, H. Li and L. Lei, *Cell. Signal.*, 2025, **134**, 111921.
13 F. Inchingolo, A. M. Inchingolo, G. Latini, L. Ferrante, I. Trilli, G. Del Vecchio, G. Palmieri, G. Malcangi, A. D. Inchingolo and G. Dipalma, *Nutrients*, 2024, **16**(1), DOI: 10.3390/nu16010113.

14 J. M. MatÉs, C. Pérez-Gómez and I. N. De Castro, *Clin. Biochem.*, 1999, **32**, 595–603.
15 H. Wei and E. Wang, *Chem. Soc. Rev.*, 2013, **42**, 6060–6093.
16 R. Ragg, A. M. Schilmann, K. Korschelt, C. Wieseotte, M. Kluenker, M. Viel, L. Völker, S. Preiß, J. Herzberger, H. Frey, K. Heinze, P. Blümler, M. N. Tahir, F. Natalio and W. Tremel, *J. Mater. Chem. B*, 2016, **4**, 7423–7428.
17 W. Zhang, S. Hu, J.-J. Yin, W. He, W. Lu, M. Ma, N. Gu and Y. Zhang, *J. Am. Chem. Soc.*, 2016, **138**, 5860–5865.
18 N. Singh, M. A. Savanur, S. Srivastava, P. D'Silva and G. Mugesh, *Angew. Chem., Int. Ed.*, 2017, **56**, 14267–14271.
19 J. Yao, Y. Cheng, M. Zhou, S. Zhao, S. Lin, X. Wang, J. Wu, S. Li and H. Wei, *Chem. Sci.*, 2018, **9**, 2927–2933.
20 Y. Liu, Y. Cheng, H. Zhang, M. Zhou, Y. Yu, S. Lin, B. Jiang, X. Zhao, L. Miao, C.-W. Wei, Q. Liu, Y.-W. Lin, Y. Du, C. J. Butch and H. Wei, *Sci. Adv.*, 2020, **6**, eabb2695.
21 D. Rajendran, A. Kannan, K. Bharathi, M. Shobha, S. Mohana, E. Reeta, N. K. S. Gowda, A. Sahoo and M. Gopi, *J. Cluster Sci.*, 2025, **36**, 158.
22 F. Ataollahi, B. Amirheidari, Z. Amirheidari and M. Ataollahi, *Biotechnol. Lett.*, 2025, **47**, 18.
23 D. F. Wang, Z. H. Yan, L. K. Ren, Y. Jiang, K. Zhou, X. P. Li, F. C. Cui, T. T. Li and J. R. Li, *Food Chem.*, 2025, **475**, 143377.
24 Y. Lin, J. Ren and X. Qu, *Acc. Chem. Res.*, 2014, **47**, 1097–1105.
25 J. Wu, X. Wang, Q. Wang, Z. Lou, S. Li, Y. Zhu, L. Qin and H. Wei, *Chem. Soc. Rev.*, 2019, **48**, 1004–1076.
26 L. Ma, Q. Zhang, J. Guo, L. Peng, P. Ma, T. Gao, G. Gou, J. Yang and W. Zuo, *ACS Appl. Mater. Interfaces*, 2025, **17**, 66391–66406.
27 Q. Zhang, L. Peng, Q. Zhang, J. Guo, N. Yu, J. Yang and W. Zuo, *ACS Appl. Mater. Interfaces*, 2025, **17**, 5942–5954.
28 Y. Cai, J. Wu, L. Peng, J. Ren, J. Yang, S. Yang, W. Zuo and J. Yang, *Chem. Eng. J.*, 2025, **522**, 167765.
29 R. Breslow, *Acc. Chem. Res.*, 1995, **28**, 146–153.
30 L. Pan, Q. He, J. Liu, Y. Chen, M. Ma, L. Zhang and J. Shi, *J. Am. Chem. Soc.*, 2012, **134**, 5722–5725.